

# Polar Dust Emission in Quasar IR SEDs and Its Correlation with Narrow Line Regions

JIANWEI LYU (吕建伟) <sup>1</sup> AND GEORGE H. RIEKE <sup>1</sup>

<sup>1</sup> *Steward Observatory, University of Arizona, 933 North Cherry Avenue, Tucson, AZ 85721, USA*

(Received Aug 1, 2022; Revised Sep 30, 2022; Accepted Oct 14, 2022)

Submitted to ApJL

## ABSTRACT

Polar dust has been found to play an important role in the mid-infrared emission of nearby Seyfert nuclei. If and how often polar dust exists among the quasar population is unknown due to the lack of spatially-resolved observations. In this Letter, we report correlations between the prominence of AGN forbidden line emission (commonly associated with the narrow line region) and the dust mid-IR energy output among the archetypal Palomar-Green quasar sample and other bright type-1 AGNs drawn from the SDSS, Spitzer and WISE archives. The AGN mid-IR color differences traced by WISE W2 ( $\sim 4.6 \mu\text{m}$ )–W3 ( $\sim 12 \mu\text{m}$ ) and W2 ( $\sim 4.6 \mu\text{m}$ )–W4 ( $\sim 22 \mu\text{m}$ ), and near-IR to mid-IR SEDs constrained with 2MASS, WISE and Spitzer data have clear trends with the relative strength of the forbidden line regions traced by the optical [O III] and mid-IR [O IV] emission lines. These observations indicate that, where the lines are strong, a large fraction of the AGN emission at  $\lambda \gtrsim 5 \mu\text{m}$  comes from dust in the forbidden line regions. We find that the widely quoted universal AGN template is a result of averaging quasar SEDs with different levels of polar dust emission above the torus output and that the typical intrinsic IR SED of compact torus dust emission alone falls with increasing wavelength past  $5 \mu\text{m}$  (in  $\nu F_\nu$ ). In addition, the association of polar dust with the forbidden lines suggests an alternative to the receding torus hypothesis for the decrease in infrared output with increasing AGN luminosity.

*Keywords:* dust, extinction — galaxies: active — galaxies: Seyfert — infrared: galaxies — quasars: general

## 1. INTRODUCTION

In the unification model of active galactic nuclei (AGNs), the mid-IR emission is assumed to originate from a compact torus-like obscuring structure surrounding the central engine (Antonucci 1993; Urry & Padovani 1995). This concept has been widely adopted to interpret the infrared emission of AGNs (e.g., Fritz et al. 2006; Nenkova et al. 2008; Stalevski et al. 2012; see reviews in e.g., Netzer 2015). Ground-based high resolution imaging of nearby Seyfert nuclei allows direct constraints on the dust morphology of AGN mid-IR emission at  $\sim 10 \mu\text{m}$  down to a few tens of parsecs (pc), and interferometry can reach pc-scale features. However, instead of a compact pc-scale torus, such observations have frequently revealed dust structures extending 10-100 pc along the polar direction (e.g., Bock et al. 2000; Radomski et al. 2003; Hönig et al. 2013; López-Gonzaga et al. 2016; Asmus et al. 2016) and challenged the classical picture.

In fact, the existence of AGN-heated dust on larger scales in the narrow line region (NLR), preferentially along the polar direction, was suggested long ago (e.g., Netzer & Laor 1993; Dopita et al. 2002) and directly revealed by, e.g., the

early spatially-resolved mid-IR observations of the archetypal type-2 AGN NGC 1068 and type-1 AGN NGC 4151 where the extended dust emission at  $\sim 10 \mu\text{m}$  is co-spatial with the NLR morphology (e.g., Bock et al. 2000; Radomski et al. 2003). Recent observations of larger AGN samples frequently report that the extended mid-IR emission is aligned with NLR position angle, suggesting this behavior is characteristic of many AGNs (e.g., López-Gonzaga et al. 2016; Asmus et al. 2016; Alonso-Herrero et al. 2021). Notably, Asmus (2019) selected AGNs with strong mid-IR [O IV] $\lambda 25.89 \mu\text{m}$  emission for mid-IR interferometry observations and found polar emission in nearly every member of the sample, supporting the association of AGN mid-IR polar emission with NLRs.

Nevertheless, addressing the prevalence of extended polar dust is difficult observationally, as mid-IR observations with sufficient spatial resolution are limited to the nearest objects with preferred inclination angles. However, Lyu & Rieke (2018) suggest that the polar dust component can leave distinct features in the AGN IR spectral energy distribution (SED) to allow its identification, and argue that the typical

NLR clouds can naturally host the dust grains responsible for the polar dust emission. If confirmed, such an association could extend our understanding of the incidence of polar dust to much more distant objects and allow new insights into the AGN IR SED variations.

In this Letter, we investigate whether there is a direct connection between the dust responsible for the AGN mid-IR emission and the gas producing the narrow line emission. § 2 summarizes the various optical and mid-IR measurements of AGNs and quasars used for our analysis. We report a correlation between the relative strengths of the AGN NLRs and the behavior of the mid-IR output in § 3. § 4 discusses how this result reshapes our understanding of various AGN properties in general.

## 2. SAMPLE, DATA AND MEASUREMENTS

Our study is focused on three samples:

- PG quasars: this sample consists of the 87  $z < 0.5$  Palomar-Green (PG) quasars selected from the Palomar Bright Quasar Survey (Schmidt & Green 1983; Boroson & Green 1992), which have rich IR photometric data from 2MASS, UKIDSS, *Spitzer*, *Herschel* and *WISE* and high-quality *Spitzer*/IRS spectra in the mid-IR. These sources have served as a foundation for quasar studies over the past four decades. In Lyu et al. (2017); Lyu & Rieke (2017), we used this dataset to study the intrinsic AGN IR SED variations of quasars in detail, laying a basis for the current work;
- SDSS quasars: To increase the sample statistics, we also select 8506 quasars from the DR7 edition of the Sloan Digital Sky Survey (SDSS) Quasar Catalog, with spectroscopy compiled by Shen et al. (2011). We require these objects to be at  $z < 0.5$  and to have measurements of [O III] and  $H\beta$ . We have identified near-to mid-IR counterparts within a search radius of  $3''$  in 2MASS and WISE for 7712 of these quasars (90.7%);
- SDSS-*Spitzer* AGNs: We also build a third type-1 AGN sample with mid-IR spectra by matching the *Spitzer*/IRS archive with the broad-line AGNs from the SDSS survey. These type-1 AGNs are identified by  $\text{FWHM}(H\alpha) \gtrsim 1200$  km/s, either in the DR7 edition of the SDSS Main Galaxy Sample (Hao et al. 2005) or the Quasar Catalog (Shen et al. 2011). The mid-IR spectra are mainly from the Combined Atlas of Sources with *Spitzer* IRS Spectra (CASSIS; Lebouteiller et al. 2011)<sup>1</sup> with some additional objects from the ATLAS project (Hernán-Caballero & Hatz-

iminaoglou 2011)<sup>2</sup>. We have visually inspected the mid-IR spectra to make sure that they have adequate signal-to-noise ratios for the  $\sim 6\text{--}30$   $\mu\text{m}$  continuum as well as the mid-IR [O IV] emission line, and do not have overwhelmingly strong PAH emission or silicate absorption features. In total, there are 209 type-1 AGNs under these criteria.

To trace the NLR, we use forbidden lines of oxygen, [O III] $\lambda 5007\text{\AA}$  and [O IV] $\lambda 25.89\mu\text{m}$ ; both lines have relatively low ionization energy and extend over large physical scales ( $\gtrsim 100$  pc) around AGNs. As both lines show correlations with the AGN luminosity (e.g., Diamond-Stanic et al. 2009; Malkan et al. 2017), basing the study on absolute line strengths is not appropriate. Instead, we normalize each of them with another AGN luminosity indicator, namely  $H\beta$  and the  $4\text{--}5$   $\mu\text{m}$  continuum (traced by the WISE W2 band)<sup>3</sup>, to remove this dependence and trace the relative strength of the NLR.

The optical emission line measurements for PG quasars are taken from Boroson & Green (1992) and for the SDSS quasars from Shen et al. (2011). The mid-IR [O IV] properties of the sample, such as line flux, FWHM and equivalent width (EW), are measured by fitting a single Gaussian function with a local continuum to the observed *Spitzer*/IRS data with our own customized code.

More detailed information on the sample as well as the relevant data and measurements are provided online at <https://github.com/karlan/AGN-MIR-SED-NLR>.

## 3. RESULTS

To characterize the AGN IR emission, we first calculate the IR colors for individual sources and later compute average SED/spectral templates for objects binned by different NLR strengths.

### 3.1. Trend of Infrared Colors with NLR Strength

To trace the significance of polar infrared emission, we adopt the WISE W2–W3 and W2–W4 color differences, since (1) W3 ( $\sim 12\mu\text{m}$ ) probes the wavelength range where the existence of polar dust is well established and (2) W4 ( $\sim 22\mu\text{m}$ ) is near the peak of the expected polar dust SED (e.g., Höning et al. 2013; Lyu & Rieke 2018).

The left panels in Figure 1 show how the WISE W2–W3 and W2–W4 colors indicate stronger mid-IR emission with

<sup>2</sup> <http://www.denebola.org/atlas/>

<sup>3</sup> The strength of the former is dominated in type-1 AGNs by the emission of broad-line regions and the latter probes the hot dust emission strength near the AGN sublimation zone, both of which trace common nuclear structures in type-1 AGNs below or near parsec scales (e.g., Kaspi et al. 2005; Lyu et al. 2019) and are believed to be approximate indicators of AGN luminosity (e.g., Malkan et al. 2017; Asmus et al. 2015).

<sup>1</sup> <https://cassis.sirtf.com/>

increasing  $[O\text{IV}]/W2$  for both the PG sample and the SDSS-Spitzer sample. Correlations are apparent in both panels. The Spearman’s rank correlation coefficients  $\rho$  in the W2–W3 bands for the PG and SDSS-Spitzer quasars are 0.476 ( $p=1.383\text{e-}05$ ) and 0.601 ( $p=6.03\text{e-}22$ ), where  $p$  is the probability of the null hypothesis that a correlation does not exist. The Spearman’s  $\rho$  in W2–W4 for PG and SDSS-Spitzer quasars are 0.382 ( $p=6\text{e-}4$ ) and 0.531 ( $p=1.282\text{e-}16$ ).

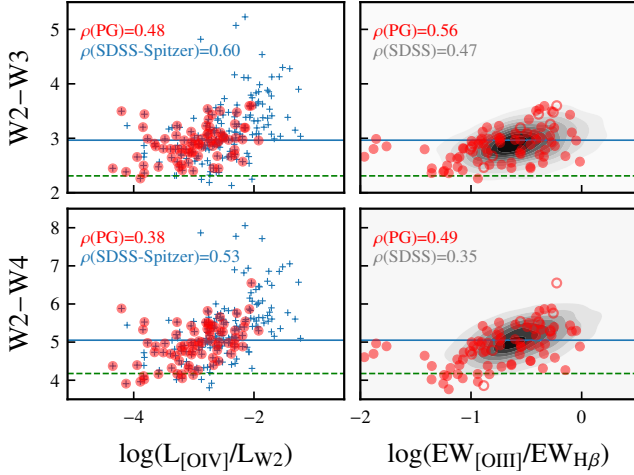


**Figure 1.** WISE colors vs.  $[O\text{IV}]25.89\mu\text{m}/W2$  luminosity ratio (left panels) and  $[O\text{III}]5007\text{\AA}/H\beta$  EW ratio (right panels). The red dots are for the PG quasar sample, with the open circles indicating the cases where galaxy emission contributes over 50% of the IR output (from Lyu et al. (2017)), the blue crosses are for the SDSS-Spitzer sample (left panels) and background grey contours are the distribution of the SDSS quasar sample (right panels). The typical 1- $\sigma$  uncertainties of these measurements are  $\lesssim 5\text{--}10\%$ . The green-dashed and blue solid lines are, respectively, the template colors of warm-dust-deficient and normal AGN templates at the average redshift of the sample. The Spearman’s rank correlation coefficients  $\rho$  of each sample are denoted in the corresponding color.

Similar AGN IR color trends also exist for the optical NLR tracer,  $\text{EW}([O\text{III}])/\text{EW}(H\beta)$ , for both PG and SDSS quasars, as presented in the right panels of Figure 1. The Spearman’s  $\rho$  values for the W2–W3 color difference for PG and SDSS quasars are 0.487 ( $p=2.98\text{e-}06$ ) and 0.349 ( $p=1.1\text{e-}239$ ), respectively. The values for W2–W4 for PG and SDSS quasars are 0.561 ( $p=0.0$ ) and 0.471 ( $p=3.459\text{e-}08$ ), respectively. For the PG sample, we have highlighted those cases with a strong host contribution in the IR with open circles, as measured in (Lyu & Rieke 2017). For quasars with  $f_{\text{host,IR}} > 0.5$ , the AGN still dominates the mid-IR by  $> 90\%$  (Lyu & Rieke 2017). That is, the influence of galaxy contamination on these trends is minimal.

### 3.2. Average SED Templates

To illustrate further how the forbidden line strength is connected with the nature of the AGN SED, we sorted the PG and SDSS-Spitzer samples into bins of  $L_{[O\text{IV}]} / L_{W2}$  and  $\text{EW}([O\text{III}]) / \text{EW}(H\beta)$  and derived the corresponding AGN templates for different relative NLR strengths. The vast majority of these objects have *Spitzer*/IRS spectra that can reveal host galaxy contamination in the mid-IR emission by the detection of the  $11.3\mu\text{m}$  PAH feature. To remove the galaxy contamination, we subtracted a Rieke et al. (2009) star-forming galaxy IR template from the observed *Spitzer*/IRS spectra to make the peak of any residual  $11.3\mu\text{m}$  PAH feature strength fall below 3- $\sigma$  flux uncertainties. As the *Spitzer* spectra only span the rest-frame  $5.5\text{--}35\mu\text{m}$ , we extended the wavelength coverage at shorter wavelengths with the photometric SEDs from 2MASS and WISE. We interpolated the IR photometry of each object in  $\log \nu - \log F_\nu$  space, smoothed the interpolated SED with a  $\Delta \log(\nu) = 0.2$  boxcar with the same wavelength grid and replaced it with the mid-IR spectra if available.

We visually investigated these SEDs and dropped any objects that (1) show abnormal SED jumps due to time variability (note that the 2MASS/WISE/Spitzer data are observed at different times); (2) have mid-IR silicate features in absorption; (3) have very strong PAH features that dominate the mid-IR emission; (4) show convincing evidence for non-thermal mid-IR emission (e.g., some BL Lac objects have a falling power-law mid-IR continuum); (5) do not have measurements of the mid-IR  $[O\text{IV}]$  line strength. After incorporating all these constraints, 177 objects were left. We grouped them into three bins for  $L_{[O\text{IV}]} / L_{W2}$  or  $\text{EW}([O\text{III}]) / \text{EW}(H\beta)$  with identical sample sizes ( $\sim 59\text{--}60$  objects), normalized each SED at rest-frame  $14.5\mu\text{m}$  where the spectrum is featureless, and computed the median average SEDs as the final templates.

In Figure 2, we show the average templates before (upper panels) and after removing the host galaxy contamination (bottom panels). Perceivable trends with  $L_{[O\text{IV}]} / L_{W2}$  and  $\text{EW}([O\text{III}]) / \text{EW}(H\beta)$  are present in all the panels. After the host galaxy removal, the resulting AGN SED templates have very weak PAH features and the continuum emission should be dominated by the AGN-heated dust. We can see clearly that the relative strength of the AGN mid-IR ( $10\text{--}30\mu\text{m}$ ) output to that at  $\sim 3\mu\text{m}$  increases with increasing  $[O\text{IV}]/W2$  ratio or  $[O\text{III}]/H\beta$  ratio. The behavior is consistent with the color trends in Figure 1, but attaches specific SEDs to the trend. In addition, the prominence of the mid-IR forbidden lines, e.g.,  $[\text{Ne II}]$ ,  $[\text{Ne III}]$ ,  $[\text{Ne V}]$  and  $[\text{S III}]$ , is also associated with an increase of mid-IR continuum strength.

### 3.3. Robustness of These Correlations

The trends in Figure 1 and Figure 2 should not be affected by extinction. Our study is focused on Type-1 to 1.5 AGNs

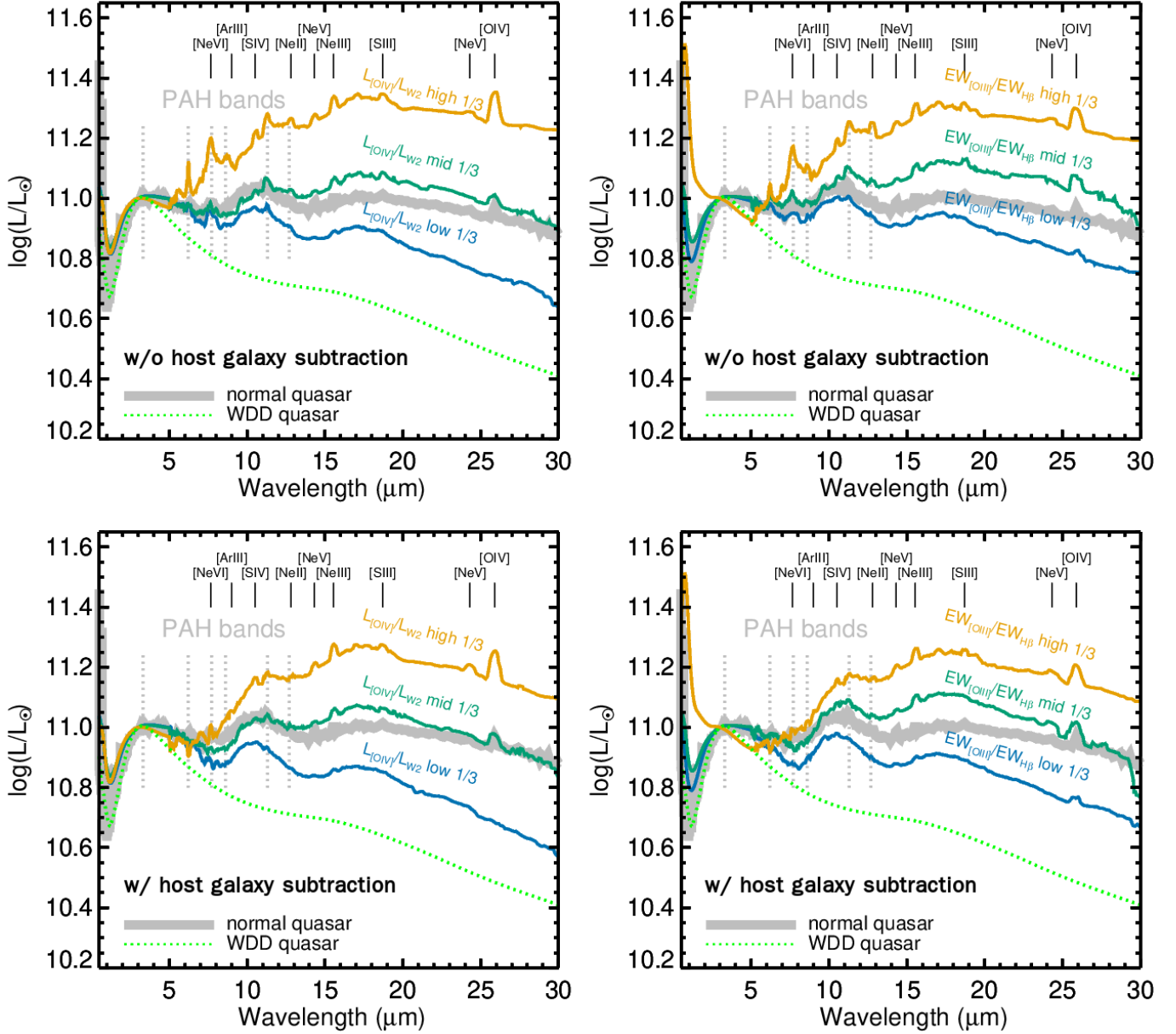


**Figure 2.** Average infrared SEDs of the sample binned by  $L_{[\text{OIV}]} / L_{W2}$  (left panels) and of  $\text{EW}([\text{OIII}]) / \text{EW}(\text{H}\beta)$  (right panels) without (top panels) and with host galaxy subtraction (bottom panels). The top 1/3, middle 1/3 and low 1/3 of the population are plotted as orange, dark green and blue solid lines. As a comparison, we also show the spectral template of the normal quasar population (thick grey line) and the broad-band SED template of the warm-dust-deficient (WDD) quasar population (light green dotted line) constructed in Lyu et al. (2017). All the templates are normalized at  $3 \mu\text{m}$  with common mid-IR emission features denoted.

where the Balmer broad lines are clearly detected and the extinction in the visible is relatively small. As the dust opacity decreases quickly from the optical to the mid-IR (e.g., Gordon et al. 2021), the expected extinction in the W2 and W4 bands and the [OIV] line would be even smaller and can be safely ignored. The W3 band does include the silicate absorption feature but the extinction over the entire broad band is still far less ( $< 6\%$ ; e.g., Rieke & Lebofsky 1985) than in the visible. The [OIII]/ $\text{H}\beta$  ratio is widely used as be-

ing roughly extinction-independent due to their close wavelengths.

The behavior of  $\text{EW}([\text{OIII}]) / \text{EW}(\text{H}\beta)$  in Figure 1 might be affected by the Baldwin Effect. As shown by e.g., Kovačević et al. (2010), the Baldwin Effect is similar for [OIII] and narrow  $\text{H}\beta$ . The broad  $\text{H}\beta$ , however, has a weak and negative Baldwin Effect. The net result would drive down [OIII]/ $\text{H}\beta$  modestly as the AGN luminosity increases. In fact, within the errors the slopes of the ratio of line flux to continuum flux are

identical for these lines, i.e., the ratio is independent of luminosity (Wilkes et al. 1999). The Baldwin Effect is less thoroughly observed for the [OIV] line, although Keremedjiev et al. (2009) observe it for other mid-infrared fine structure lines. Again, it will drive down the ratio of the [OIV] line to W2 with increasing luminosity. However, in both cases since the shapes of the infrared SEDs of AGNs, e.g., W2 – W3 or W2 – W4, do not correlate with luminosity<sup>4</sup>, the effect will increase the scatter in Figure 1 but should not contribute to the correlations.

Figure 3 compares the redshift and AGN luminosity distributions of the sub-samples used to compute the average templates in Figure 2. No statistical difference is seen for the sample redshifts. However, the AGN luminosity shows a negative trend with both  $L_{[\text{OIV}]} / L_{W2}$  and  $\text{EW}([\text{OIII}]) / \text{EW}(\text{H}\beta)$ . As discussed in § 4.3, the NLR strength does have some dependence on the AGN luminosity and thus this AGN luminosity difference is a result of sub-sample definition. For the AGN mid-IR SED and NLR strength correlations presented above, however, we used the ratios of two luminosity indicators to take out this luminosity effect. As a result, our interpretation is not influenced by the sample luminosity.

Lastly, the choice of host galaxy template would not affect our results as the changes of the AGN color after the galaxy subtraction are small, as shown in Figure 1.

In conclusion, none of the factors mentioned above can explain the correlations.

#### 4. DISCUSSION

Previous work by Zhang et al. (2013) reported a correlation between the covering factor for the dust around an AGN and the strength of the wing of the  $[\text{OIII}]\lambda 5007\text{\AA}$  line relative to the bolometric luminosity. The results obtained in this work agree generally with that study and our analysis reveals a strong correlation between the relative AGN mid-IR energy output and the relative strength of the NLR emission; i.e., the more prominent the NLR region, the stronger the dust emission in the mid-IR. As shown below, this result expands our understanding of the variations in AGN SEDs we have described previously and can provide new insights to AGN behavior.

##### 4.1. Quasar IR SEDs

In Lyu et al. (2017), we found two major variations in intrinsic IR SEDs compared with “normal” AGNs (e.g., that of Elvis et al. 1994): (1) the warm-dust-deficient (WDD) case has similar hot dust emission at 1–3  $\mu\text{m}$  as normal objects but is weaker in the mid-IR; and (2) the hot-dust-deficient

(HDD) case has weak dust emission throughout the near- and mid-IR. As shown in Figure 1, the WDD template represents the smallest W2–W3 and W2–W4 color differences seen in quasars; it also appears to be the limiting case for a weak NLR. This suggests that the WDD template represents the compact dust emission associated with the classical torus alone. In Lyu & Rieke (2018) we showed that the normal AGN SED can be approximately reproduced by adding polar dust emission above the WDD template with an effective optical depth  $\tau_{\text{pol}} \sim 0.8$ . Consistent with this possibility, our semi-empirical SED fitting for all three type-1 AGNs with polar dust constraints from mid-IR interferometry (NGC 3783, ESO 323-77 and NGC 4507) suggested that their nuclear dust emission SED could be WDD.

Particularly for the comparison based on the [OIV] line, the SEDs for weak line emission drop toward longer wavelengths in Figure 2 similarly to the behavior of the HDD and WDD templates. In comparison, the SED for strong line emission lies above even the “normal” template of Lyu et al. (2017). Based on this evidence, we suggest that a large fraction, if not all, the excess emission above the WDD template comes from relatively extended dust associated with the NLR.

The average quasar SEDs derived in the literature show similar dust continua that are described by the normal template and have little evolution with redshift (e.g., see references in Lyu & Rieke 2018). Given the discussion in the preceding paragraph, this suggests that a large fraction of quasars have a moderate level of polar dust emission. Some 60–70% of the PG quasars have excess AGN dust emission above the WDD template and the average relative fraction of this hypothetical extended dust emission is  $\sim 50\%$  at  $\sim 10 \mu\text{m}$ , from the comparison of normal and WDD AGN templates (see Figure 2 in Lyu et al. 2017). As most works computing average quasar templates do not differentiate SED properties, the normal-like AGN templates are a result of averaging AGN SEDs with different levels of extended NLR dust emission and different intrinsic torus SEDs, including cases that are relatively brighter in the mid-infrared than even the normal template. This situation is illustrated in Shang et al. (2011), Figure 10, and Lyu & Rieke (2018), Figures 6 & 7. The success of the normal template in SED fitting and decomposition derives directly from its being an overall average, not because it represents all AGNs accurately.

A deeper understanding of the dusty surrounds of AGNs requires decoding the roles of the circumnuclear tori and the polar dust. High resolution imaging (e.g., Bock et al. 2000; Radoski et al. 2003; Alonso-Herrero et al. 2021) and interferometry (e.g., Hönig et al. 2013; Asmus 2019; Isbell et al. 2022) of nearby AGNs have established that the mid-infrared emission of many of them is dominated by polar dust often shown to be associated directly with their NLRs, rather than

<sup>4</sup> Although the strength of the infrared SED relative to the visible does correlate with luminosity, see § 4.3.

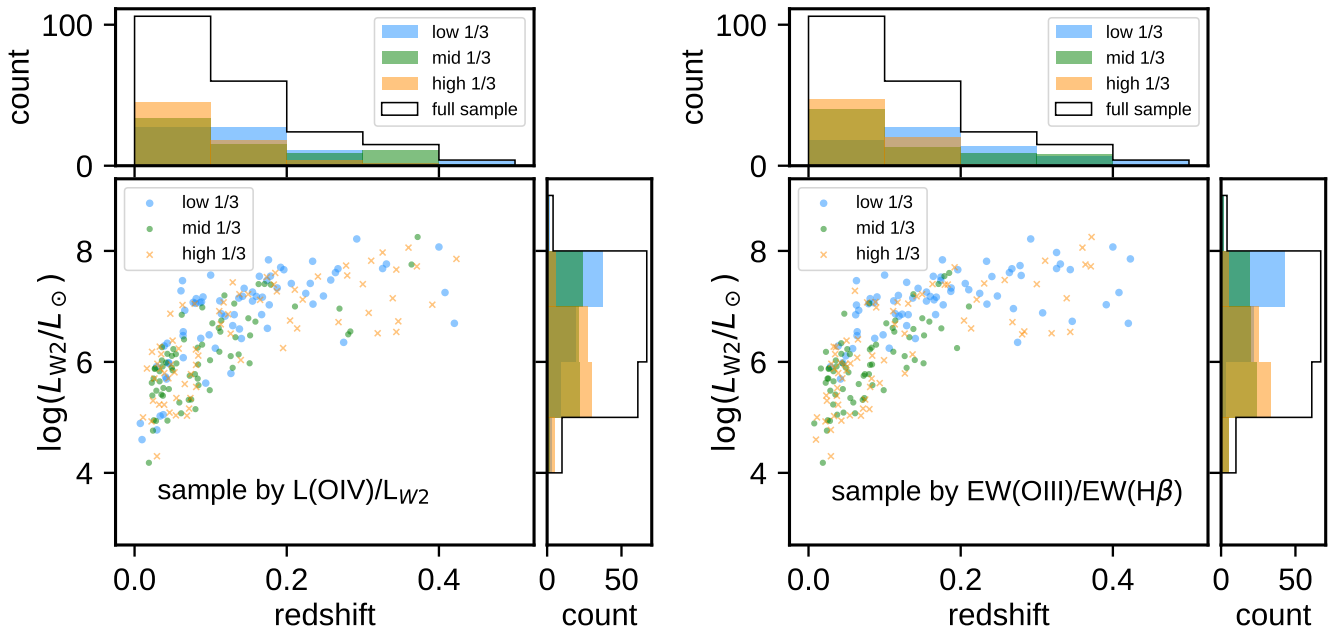


**Figure 3.** Redshifts and luminosity (traced by  $L_{W2}$ ) distribution of the sub-samples used to compute AGN templates in Figure 2.

being solely the output of compact ( $\lesssim 1 - 10$  pc) tori. Extending such studies to a significant number of distant and luminous AGNs is not feasible, but the association of mid-infrared color differences with the relative strength of the forbidden oxygen lines shows that a similar situation holds for them. This association is not predicted at all by traditional torus models.

#### 4.2. Role of the NLR and of Winds

From a study of  $\sim 4200$  type-1 AGNs from SDSS, Zhang et al. (2013) also reported correlations between the mid-IR dust emission strength and optical [O III] emission, in their case both normalized by the AGN bolometric luminosity. They decomposed the [O III] emission profiles into core and wing components and found that the correlations are driven by the wing component rather than the core. However, we find similar or even higher correlation coefficients for the entire [O III] emission line, possibly because we compare the W3 and W4 fluxes with the W2 one, i.e., testing the shape of the mid-IR SED rather than the role of the mid-IR in the total luminosity.

Zhang et al. (2013) concluded that dusty outflows launched near the torus, not the more extended NLR, contribute most of the AGN mid-IR emission. However, observations of nearby AGNs such as NGC 1068 (Bock et al. 2000), NGC 4151 (Radomski et al. 2003), and many more (Alonso-Herrero et al. 2021) show that a substantial fraction of the  $10 \mu\text{m}$  emission comes from regions well removed from the nucleus, up to tens of pc for luminous systems. This behavior is consistent with our finding substantial correlations with

the integrated oxygen line strengths rather than just the broad components.

Baron & Netzer (2019) also used the [O III] and WISE data to explore the role of winds. Their sample of AGNs was matched closely in narrow [O III] luminosity between cases with only narrow [O III] and those with a significant broad component in the [O III] line profile, indicative of winds. They compare color differences in the WISE bands for these two samples. There is a convincing case for the systems with winds to have stronger emission in W4 ( $22 \mu\text{m}$ ) than those without but mixed results for a stronger excess in W3 ( $12 \mu\text{m}$ ).

Alonso-Herrero et al. (2021) compare high resolution images at  $\sim 10 \mu\text{m}$  with ALMA images of submm emission by dust and the distribution of CO (3-2). The variety of configurations and overall complexity undermines any universal and simple interpretation. They find in the most extended cases that the  $10 \mu\text{m}$  emission has sizes of  $50 - 160$  pc, much less than the kpc sizes derived from the models of Baron & Netzer (2019). However, the groundbased data are insensitive to low surface brightness extended source components.

The polar dust emission seen by mid-IR interferometry is on a different scale from the  $50 - 160$  pc dusty narrow line regions seen in imaging. However, as pointed out by Lyu & Rieke (2018), this extended dust structure is expected to have a temperature gradient that makes the dust emission size change as a function of the observed wavelength. In fact, a simple SED model featuring diffuse dust distributed over  $100$  pc scales proposed in the same work matched the observed polar dust sizes at  $\sim 10 \mu\text{m}$ . This argument is illustrated

by the GRAVITY (Gravity Collaboration et al. 2020), MATISSE (Gómez Rosas et al. 2022), and imaging Bock et al. (2000) observations of NGC 1068. The first reveals a ring-like structure at K-band ( $\sim 2.2 \mu\text{m}$ ), the second shows dust emission at  $\sim 4\text{--}12 \mu\text{m}$  mostly consistent with a polar wind, and the third shows extended emission on 100 pc scales to the full extent of the bright forbidden line region seen at  $12.5 \mu\text{m}$  and suggests even greater extent at  $24.5 \mu\text{m}$ . Further extent at low surface brightness at  $12.8 \mu\text{m}$  is also shown by Galliano et al. (2005).

The questions about the interpretation of the extended mid-IR emission should be answered by JWST/MIRI observations, which will obtain images of sufficient resolution and surface brightness sensitivity out through  $21 \mu\text{m}$ , thus including the spectral range where, from the work of Baron & Netzer (2019), the wind-associated emission should be brightest.

#### 4.3. Dust Covering Factor vs Luminosity

From comparing AGN IR templates, we can estimate the dust covering factor of the NLR for a typical quasar with a normal IR SED. From the calculations in Lyu et al. (2017); Lyu & Rieke (2017), the ratio of dust emission to the AGN accretion disk luminosity  $L_{\text{NLRdust,IR}}/L_{\text{accr.disk}}$  is 0.53 and 0.37 for the normal and WDD templates, respectively. Assuming the WDD template represents the SED of the compact torus and any excess IR emission is from the NLR, this would indicate about 37% and 15% of the accretion disk emission is obscured, i.e. “covered”, by the equatorial torus and the polar NLR dust, respectively. In other words, the torus vs. polar dust emission luminosity is about 2.3:1 for the normal quasar population.

Although there is little evidence for a strong redshift evolution of AGN IR SED behavior, the relative strength of the overall AGN mid-IR emission is commonly found to decrease with source luminosity (e.g., Maiolino et al. 2007; Roseboom et al. 2013). In the past, a so-called receding torus has frequently been invoked to explain this observation (e.g. Lawrence 1991). It posits that the torus dust is destroyed by the increasing AGN luminosity, resulting in less IR emission. Given the very likely connection between the AGN mid-IR emission and dusty NLR, this behavior is likely to arise instead from the well-established reduction in the NLR prominence with increasing AGN luminosity (e.g., Netzer et al. 2006; Stern & Laor 2012).

To illustrate this possibility, we present the luminosity dependence of the [O III] relative strength and IR relative excess emission above the WDD template for the SDSS quasar sample in Figure 4. Both parameters show clear negative trends with AGN luminosity with Spearman’s rank correlation coefficient values  $\rho = -0.42$  ( $p < 1e-4$ ) and  $\rho = -0.21$  ( $p < 1e-4$ ), respectively. The Baldwin Effect on [O III]/H $\beta$  is inadequate to account for any significant part of the behavior in the up-

per panel of the figure (see § 3.3). Fitting these data by linear regression, we find the slopes of the correlations are consistent within uncertainties. In conjunction with the correlations between these two properties shown in Figure 1, this behavior also provides further evidence for the mid-IR emission of lower luminosity AGNs having a substantial component from their NLRs.

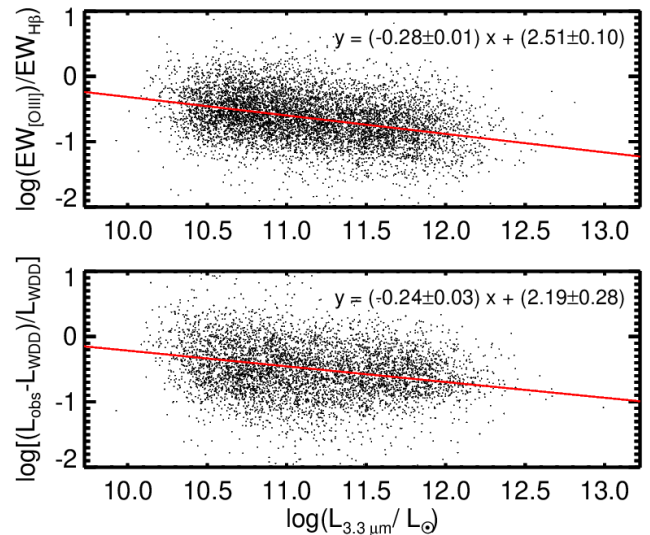


**Figure 4.** Luminosity dependence of the AGN narrow-line emission strength and IR excess emission. For each quasar, we have interpolated and smoothed the observed SEDs, subtracted a WDD AGN template with the normalization at rest-frame  $3.3 \mu\text{m}$ , and computed the relative excess luminosity at  $5\text{--}25 \mu\text{m}$  as  $(L_{\text{obs}} - L_{\text{WDD}})/L_{\text{WDD}}$ . The red lines show the linear regressions of the data points with the fitted relations reported in the top-right corner of each panel.

## 5. SUMMARY

We have demonstrated a correlation between the relative strengths of the optical [O III] and mid-IR [O IV] lines and the AGN mid-IR color or SED shape. This indicates that, on average, AGNs with strong forbidden line emission also have a large fraction of emission at  $\lambda > 5 \mu\text{m}$  emitted by dust in the forbidden line regions. The AGNs with weak forbidden lines have infrared SEDs that drop past  $5 \mu\text{m}$  with increasing wavelength in  $\nu F_\nu$ , compared with the flat or rising SEDs on average for those with strong forbidden lines. This difference suggests that the compact circumnuclear torus emits a SED similar to the weak forbidden line case, i.e., as in the warm dust deficient (WDD) template of Lyu et al. (2017). It also implies that  $\sim 60\text{--}70\%$  of the optically-selected blue quasars have a significant level of polar dust emission with a relative contribution at  $\sim 10 \mu\text{m}$  about 50% on average above the WDD template. For a normal quasar with a typical average SED, the fraction of accretion disk UV-optical emission

transferred into the infrared is estimated to be 37% and 15% by the equatorial torus and polar dusty NLR, respectively.

We also find that the decrease of the so-called dust covering factor with the increase of AGN luminosity is likely to be a result of the reduction of the forbidden line region rather than a receding torus.

We expect upcoming JWST/MIRI spatially-resolved observations of nearby AGNs to greatly advance our understanding of the extended dust structures surrounding AGNs.

We thank for anonymous referee for the comments and suggestions. This work was supported by NASA grants NNX13AD82G and 1255094.

## REFERENCES

- Alonso-Herrero, A., García-Burillo, S., Hönic, S. F. et al. 2021, *A&A*, 652, A99, doi = 10.1051/0004-6361/202141219,
- Antonucci, Robert 1993, *ARA&A*, 31, 473, doi = 10.1146/annurev.aa.31.090193.002353,
- Asmus, D. 2019, *MNRAS*, 489, 2177. doi:10.1093/mnras/stz2289
- Asmus, D., Gandhi, P., Hönic, S. F., Smette, A., & Duschl, W. J. 2015, *MNRAS*, 454, 766
- Asmus, D., Hönic, S. F., & Gandhi, P. 2016, *ApJ*, 822, 109. doi:10.3847/0004-637X/822/2/109
- Baron, D. & Netzer, H. 2019, *MNRAS*, 482, 3915. doi:10.1093/mnras/sty2935
- Bock, J. J., Neugebauer, G., Matthews, K., et al. 2000, *AJ*, 120, 2904. doi:10.1086/316871
- Boroson, Todd A. and Green, Richard F., 1992, *ApJS*, 80, 109, doi = 10.1086/191661,
- Diamond-Stanic, Aleksandar M., Rieke, George H., & Rigby, Jane R. 2009, *ApJ*, 698, 623-631, doi = 10.1088/0004-637X/698/1/623
- Dopita, M. A., Groves, B. A., Sutherland, R. S., et al. 2002, *ApJ*, 572, 753. doi:10.1086/340429
- Elvis, Martin, Wilkes, Belinda J., McDowell, Jonathan C. et al. *ApJS*, 95, 1
- Fritz, J., Franceschini, A., & Hatziminaoglou, E. 2006, *MNRAS*, 366, 767. doi:10.1111/j.1365-2966.2006.09866.x
- Galliano, E., Pantin, E., Alloin, D., & Lagage, P. O. 2005, *MNRAS*, 363, L1
- Gámez Rosas, V., Isbell, J. W., Jaffe, W., et al. 2022, *Nature*, 602, 403. doi:10.1038/s41586-021-04311-7
- Gordon, K. D., Misselt, K. A., Bouwman, J., et al. 2021, *ApJ*, 916, 33. doi:10.3847/1538-4357/ac00b7
- Gravity Collaboration, Pfuhl, O., Davies, R., et al. 2020, *A&A*, 634, A1. doi:10.1051/0004-6361/201936255
- Hao, L., Strauss, M. A., Tremonti, C. A., et al. 2005, *AJ*, 129, 1783. doi:10.1086/428485
- Hernán-Caballero, A. & Hatziminaoglou, E. 2011, *MNRAS*, 414, 500. doi:10.1111/j.1365-2966.2011.18413.x
- Hönic, S. F. 2019, *ApJ*, 884, 171. doi:10.3847/1538-4357/ab4591
- Hönic, S. F. and Kishimoto, M. and Tristram, K. R. W. et al. 2013, *ApJ*, 771, 87, doi = 10.1088/0004-637X/771/2/87
- Isbell, J.W., Meisenheimer, K., Pott, J.-U. 2022, arXiv:2205.01575
- Kaspi, S., Maoz, D., Netzer, H., et al. 2005, *ApJ*, 629, 61. doi:10.1086/431275
- Keremedjiev, Mark, Hao, Lei, & Charmandaris, Vassilis 2009, *ApJ*, 690, 1105. doi = 10.1088/0004-637X/690/2/1105,
- Kovačević, J., Popović, L. Č., & Dimitrijević, M. S. 2010, *ApJS*, 189, 15. doi:10.1088/0067-0049/189/1/15
- Lawrence, A. 1991, *MNRAS*, 252, 586. doi:10.1093/mnras/252.4.586
- Lebouteiller, V., Barry, D. J., Spoon, H. W. W., et al. 2011, *ApJS*, 196, 8. doi:10.1088/0067-0049/196/1/8
- López-Gonzaga, N., Burtscher, L., Tristram, K. R. W., et al. 2016, *A&A*, 591, A47. doi:10.1051/0004-6361/201527590
- Lyu, J., Rieke, G. H., & Shi, Y. 2017, *ApJ*, 835, 257. doi:10.3847/1538-4357/835/2/257
- Lyu, J. & Rieke, G. H. 2017, *ApJ*, 841, 76. doi:10.3847/1538-4357/aa7051
- Lyu, J. & Rieke, G. H. 2018, *ApJ*, 866, 92. doi:10.3847/1538-4357/aae075
- Lyu, J., Rieke, G. H., & Smith, P. S. 2019, *ApJ*, 886, 33. doi:10.3847/1538-4357/ab481d
- Lyu, J. & Rieke, G. H. 2022, *Universe*, 8, 304. doi:10.3390/universe8060304
- Maiolino, R., Shemmer, O., Imanishi, M., et al. 2007, *A&A*, 468, 979. doi:10.1051/0004-6361:20077252
- Malkan, Matthew A. and Jensen, Lisbeth D. and Rodriguez, David R. and Spinoglio, Luigi and Rush, Brian 2017, *ApJ*, c846, 102, doi = 10.3847/1538-4357/aa8302,
- Nenkova, M., Sirocky, M. M., Nikutta, R., et al. 2008, *ApJ*, 685, 160. doi:10.1086/590483
- Netzer, H. & Laor, A. 1993, *ApJL*, 404, L51. doi:10.1086/186741
- Netzer, H., Mainieri, V., Rosati, P., et al. 2006, *A&A*, 453, 525. doi:10.1051/0004-6361:20054203
- Netzer, H. 2015, *ARA&A*, 53, 365. doi:10.1146/annurev-astro-082214-122302
- Radomski, J. T., Piña, R. K., Packham, C., et al. 2003, *ApJ*, 587, 117. doi:10.1086/367612
- Rieke, G. H. & Lebofsky, M. J. 1985, *ApJ*, 288, 618. doi = 10.1086/162827
- Rieke, G. H., Alonso-Herrero, A., Weiner, B. J., et al. 2009, *ApJ*, 692, 556. doi:10.1088/0004-637X/692/1/556



- Roseboom, I. G., Lawrence, A., Elvis, M., et al. 2013, MNRAS, 429, 1494. doi:10.1093/mnras/sts441
- Schmidt, M. & Green, R. F. 1983, ApJ, 269, 352. doi:10.1086/161048
- Shang, Zhaohui, Brotherton, Michael S., Wills, Beverley J. et al. 2011, ApJS, 196, 1
- Shen, Y., Richards, G. T., Strauss, M. A., et al. 2011, ApJS, 194, 45. doi:10.1088/0067-0049/194/2/45
- Stalevski, Marko, Fritz, Jacopo, Baes, Maarten, Nakos, Theodoros, & Popović, Luka 2012, MNRAS, 420, 2756, doi = 10.1111/j.1365-2966.2011.19775.x,
- Stern, J. & Laor, A. 2012, MNRAS, 426, 2703. doi:10.1111/j.1365-2966.2012.21772.x
- Urry, C. Megan & Padovani, Paolo 1995, PASP, 107, 803 doi = 10.1086/133630
- Wilkes, B. J., Kuraszkiewicz, J., Green, P. J., et al. 1999, ApJ, 513, 76. doi:10.1086/306828
- Zhang, K., Wang, T.-G., Yan, L., et al. 2013, ApJ, 768, 22. doi:10.1088/0004-637X/768/1/22